RESEARCH ARTICLE

Internal calibration for opportunistic computed tomography muscle density analysis

Ainsley C. J. Smith[1,2,3], Justin J. Tse[2,3], Tadiwa H. Waungana[1,2,3], Kirsten N. Bott[2,3], Michael T. Kuczynski[1,2,3], Andrew S. Michalski[1,2,3], Steven K. Boyd[1,2,3], Sarah L. Manske[1,2,3]*

1 Biomedical Engineering Graduate Program, University of Calgary, Alberta, Canada, 2 Department of Radiology, Cumming School of Medicine, University of Calgary, Alberta, Canada, 3 McCaig Institute for Bone and Joint Health, University of Calgary, Alberta, Canada

* smanske@ucalgary.ca

Abstract

Introduction

Muscle weakness can lead to reduced physical function and quality of life. Computed tomography (CT) can be used to assess muscle health through measures of muscle cross-sectional area and density loss associated with fat infiltration. However, there are limited opportunities to measure muscle density in clinically acquired CT scans because a density calibration phantom, allowing for the conversion of CT Hounsfield units into density, is typically not included within the field-of-view. For bone density analysis, internal density calibration methods use regions of interest within the scan field-of-view to derive the relationship between Hounsfield units and bone density, but these methods have yet to be adapted for muscle density analysis. The objective of this study was to design and validate a CT internal calibration method for muscle density analysis.

Methodology

We CT scanned 10 bovine muscle samples using two scan protocols and five scan positions within the scanner bore. The scans were calibrated using internal calibration and a reference phantom. We tested combinations of internal calibration regions of interest (e.g., air, blood, bone, muscle, adipose).

Results

We found that the internal calibration method using two regions of interest, air and adipose or blood, yielded accurate muscle density values (< 1% error) when compared with the reference phantom. The muscle density values derived from the internal and reference phantom calibration methods were highly correlated ($R^2 > 0.99$). The coefficient of variation for muscle density across two scan protocols and five scan positions was significantly lower for internal calibration (mean = 0.33%) than for Hounsfield units (mean = 6.52%). There was no

difference between coefficient of variation for the internal calibration and reference phantom methods.

Conclusions

We have developed an internal calibration method to produce accurate and reliable muscle density measures from opportunistic computed tomography images without the need for calibration phantoms.

Introduction

Muscle weakness is associated with physical impairment, reduced quality of life, and mortality [1,2]. Computed tomography (CT) is a widely used clinical imaging modality that can be utilized to evaluate muscle degeneration through quantitative measures of muscle cross-sectional area and density. Muscle cross-sectional area is an indicator of muscle health that is correlated with measures of muscle function (e.g., handgrip strength, knee extension strength, short physical performance battery scores) and can be used to predict health outcomes (e.g., frailty, length of hospital stay) [3–6]. However, structural alterations, such as fat infiltration, may result in muscle cross-sectional area values underestimating changes in muscle function and muscle strength. Fat content within muscle structures can be evaluated through measurements of muscle density since fat infiltration leads to lower density muscle [7–11]. Lower muscle density in the lumbar region and the lower limbs is correlated with reduced muscle strength [3,12,13], and can be combined with measures of muscle cross-sectional area for a more comprehensive assessment of muscle health.

Muscle cross-sectional area and density can be assessed through CT imaging. Chest and abdominal CT images are frequently acquired in hospital settings for clinical diagnoses and these clinically acquired CT scans have been repurposed to investigate muscle cross-sectional area, and muscle attenuation as a surrogate for density, at the level of the lumbar vertebrae without exposure to additional ionizing radiation [14–17]. While density can be inferred from the X-ray attenuation or grey-scale value in the CT images, natively represented in Hounsfield units (HU), these values are dependent on the X-ray energy, photon flux, object position within the scanner bore, spatial resolution, beam hardening, and other artifacts [11,18–23]. This makes it challenging to reliably compare HU as a proxy for muscle density between different scanners and scan protocols. A standard solution for bone mineral density (BMD) assessment is to calibrate HU to bone analogous material density values using phantoms made with materials of known dipotassium phosphate or calcium hydroxyapatite (HA) densities [24,25]. Previous research has used BMD phantoms to successfully quantify muscle and lipid composition with a semi-automatic segmentation method based on histograms and anatomical location [23,26]. However, the use of BMD phantoms yield mineral density values in mg of dipotassium phosphate or calcium hydroxyapatite per cm^3 [27], whereas muscle is largely composed of water. Muscle density values in g/cm^3 of water could be more intuitively interpreted. However, water-based reference phantoms are not widely available due to challenges in mimicking soft tissues with shelf-s\ materials and absence of consensus of appropriate materials [28].

As an alternative to phantoms, internal density calibration techniques have been developed to convert HU to BMD values [29–32]. These methods have been developed for opportunistic BMD analysis because phantoms are not typically included in clinical CT scans or used for

clinical diagnoses. Internal density calibration involves selecting regions of interest (ROIs) of tissues (e.g., bone, blood, muscle, adipose, air) as reference materials. Some methods calibrate HU values of these ROIs to previously determined tissue-equivalent reference values [29–31]. However, a potentially more robust method involves estimating the effective scan energy using mass attenuation values of materials within the scan and then deriving the relationship between HU and material density [32]. Unfortunately, it is unknown whether BMD internal calibration methods are applicable to muscle density analysis since muscle attenuates X-rays to a lesser extent than bone. To date, there has yet to be an internal calibration method developed or validated for quantitative muscle density analysis.

The objective of this study was to design and validate an internal density calibration technique to directly measure muscle density from CT images. The basis of this internal calibration method relies upon a previously validated method for BMD [32]. Using bovine tissue samples, we sought to test the optimal combination of ROIs for muscle density analysis using the internal calibration method, as well as to compare the internal calibration method with the reference phantom calibration method. We hypothesized that our internal calibration method would be comparable to the reference phantom calibration method and would be a more robust measure of muscle density than native HU.

Methodology

Imaging

We used a standardized scan setup composed of muscle, cortical bone, adipose, blood, and a reference phantom, as shown in Fig 1. We scanned 10 bovine muscle samples which were acquired, stored, and scanned under the same conditions. The sample size was selected to
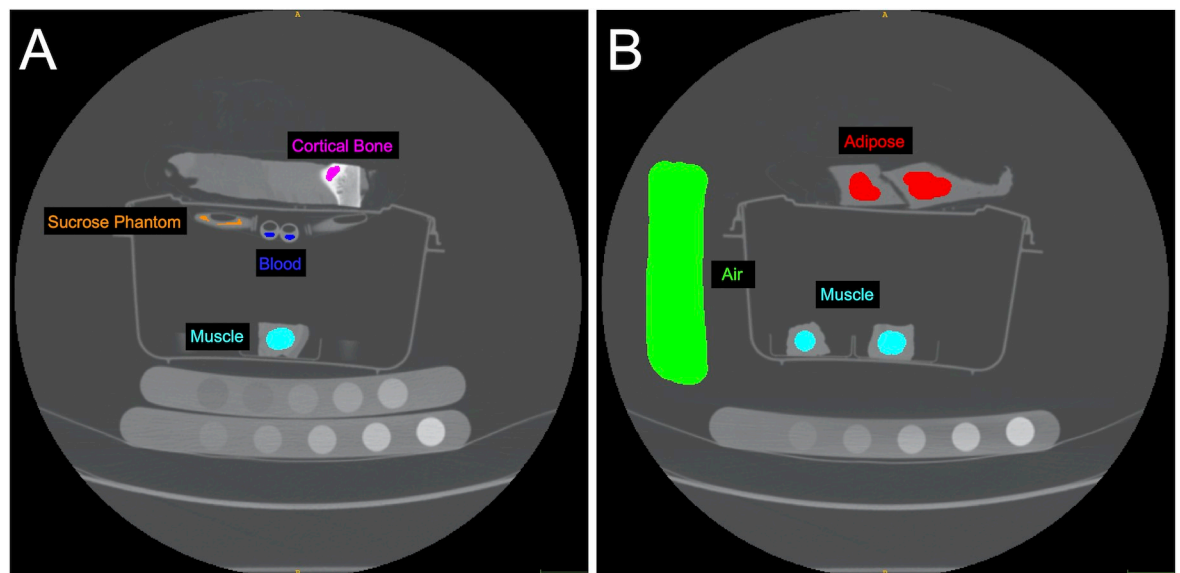
Fig 1. Computed tomography (CT) image showing the reconstructed field of view (36 cm diameter). Internal calibration regions of interest (ROIs) (air, muscle, adipose, bone, blood) were selected in the axial plane. The scan included various tissue samples, a custom sucrose water phantom, and two traditional bone phantoms (Bone Density Calibration Phantom BDC-6, QRM GmbH; Model 3 CT Calibration Phantom, Mindways Inc.). The (hydroxyapatite) HA bone phantom was used to validate the sucrose water phantom (S1 Fig). A) Axial slice including cortical bone, blood, one of the ten muscle samples, and the sucrose water phantom. B) Axial slice including adipose, air, and two of the ten muscle samples. Note that the ten muscle samples were all included in the scan, although they are not all visible in the slices shown.

https://doi.org/10.1371/journal.pone.0273203.g001

Fig 2. Muscle sample positioning. The muscle samples were scanned at five different positions within the scanner bore (70 cm diameter): left, right, top, bottom, and centre. The position of the samples was altered by adjusting the table positioning. Note that the scan setup was approximately 19 cm in height and could therefore be moved into different positions by adjusting table positioning.

https://doi.org/10.1371/journal.pone.0273203.g002

provide a range of fat infiltration. Bovine bone, bovine adipose, and swine blood were included in these scans and used as ROIs for the internal calibration method. Swine blood was used instead of bovine blood as it is more readily available as a fresh sample. As muscle density phantoms are not widely available, we included a custom sucrose water phantom consisting of five vials of sucrose water concentrations with densities of 1.00g/ml, 1.01g/ml, 1.04g/ml, 1.06g/ml, and 1.11g/ml. We scanned the muscle samples, ROI samples, and phantoms (sucrose water phantom; HA Bone Density Calibration Phantom BDC-6, QRM GmbH; Dipotassium Phosphate Model 3 CT Calibration Phantom, Mindways Inc.) using a clinical CT scanner (GE Revolution HD GSI, GE Healthcare, Chicago, USA). The HA bone phantom was used for comparison with BMD calibration [23]. We used two different scan protocols (abdominal kidney, urine, bladder (KUB) thins protocol and chest mediastinum protocol) and five different object positions (right, left, top, bottom, centre, as shown in Fig 2) to test the reliability of the internal calibration method across different scan conditions. These scan protocols were selected because they are commonly used in the clinical setting [33,34]. The KUB thins protocol was performed with 120 kVp, 99 mAs, 1.250 mm slice thickness, 1.37 mm spiral pitch factor, and was reconstructed with a standard convolution kernel. The chest mediastinum protocol was performed with 120 kVp, 90 mAs, 0.625 mm slice thickness, and 0.98 mm spiral pitch factor, and was reconstructed with a standard convolution kernel. All scans were acquired on the same day to reduce the effect of CT scanner fluctuation over time. The CT scanner undergoes quality control daily. Ethics approval was not required for this study as only commercial meat products were used and there was no contact with live animals.

Calibration

We used the internal calibration approach previously described [32] (https://github.com/Bonelab/Ogo) as a basis and developed an approach specific for muscle. This approach relates the mass attenuation coefficients attained from the National Institute of Standards and Technology (www.nist.gov) and the measured HU of internal ROIs (blood, bone, air, fat, and muscle) to estimate the effective scan energy [32]. The relationship between HU and water equivalent density is then computed through an optimization process that estimates the effective scan energy by iteratively relating the mass attenuation coefficients and HU values for each selected ROI [32]. We optimized the internal calibration method for muscle density analysis by determining the effects of different combinations of material ROI selection on the output muscle density values compared with those derived from the reference sucrose water phantom calibration method. We selected ROIs for air, blood, muscle, adipose and cortical bone regions throughout the scan in the axial plane (Fig 1). We compared internal calibration based on 1) all material ROIs (air, adipose, blood, muscle, bone) as per the method described in Michalski et al. [32]; 2) air, adipose, blood, muscle; 3) air, adipose, blood; 4) air, blood; and 5) air, adipose. We added the output of a water-equivalent density image for muscle density analysis, as the original image processing pipeline only included a dipotassium phosphate-equivalent density image output. The 10 scans (2 protocols, 5 positions) were each individually calibrated using the internal calibration method based on the material ROI combinations described above, the reference sucrose water phantom, and the HA bone phantom. For the reference sucrose water phantom calibration method, observed HU values were rescaled with the linear equation derived from the calculated densities of the sucrose vials, based on the known concentration of sucrose. For the HA bone phantom calibration method, the linear equation was derived from the density of the HA rods. All calibration methods involved manually segmenting the bovine muscle samples in ITK-SNAP V3.8.0 [22], a medical image visualization and analysis software, and converting the observed HU into muscle density values (g/cm^3 or mgHA/cm^3). To accurately assess the reliability of the calibration methods across scan conditions, we used image registration (aligned the images over top of one another) to ensure that muscle density was measured at the same ROI location for all 10 scans. Image registration was performed using an initial alignment of images through landmark based rigid 3D transformation, followed by a final alignment based on optimizing mutual information between images [35]. All image analysis was conducted using ITK-SNAP V3.8.0 [22] and Python 3.6.10 and 3.8.5 with numpy 1.20.3 [36], VTK 9.0.1 [37], and SimpleITK 2.0.2 [38] libraries.

Statistical analysis

Statistical analyses were performed using R (version 4.1.0) and RStudio (Version 1.4.1106). Linear regression was performed to compare muscle density values derived from the internal calibration method with those derived from the reference sucrose water phantom and the HA bone phantom method. Bland-Altman analysis was conducted to estimate the mean bias associated with the internal calibration method when compared with the reference sucrose water phantom method and to assess the performance of the internal calibration method when different ROI combinations were used. Linear regression was performed to assess any association between bias and the magnitude of density. Lastly, the coefficient of variance (CV) values for muscle density of each sample across the 10 scan conditions was calculated. The mean CV for the internal calibration method, the reference sucrose water phantom calibration method, and native HU were compared using within-subjects ANOVA and post-hoc analysis with Bonferroni. Statistical significance was set to $p < 0.05$.

Results

The mean muscle density and standard deviation for the 10 samples was 1.0636 (±0.0086) g/cm^3 as derived from the internal calibration method (air and adipose ROIs) and 1.0694 (±0.0086) g/cm^3 as derived from the reference sucrose phantom calibration method, acquired from the chest scan positioned in the centre of the scanner bore. The mean HU and standard deviation for the 10 samples was 57.1077 (±8.5507), acquired from the chest scan positioned in the centre of the scanner bore. We found that the exclusion of bone as a material ROI in the internal calibration process dramatically reduced the error of the derived muscle density values when compared to the reference sucrose water phantom calibration derived muscle density values (bone included: mean error = -0.055, 95% Limits of Agreement (95%LOA) = 0.0020; bone excluded: mean error = -0.004, 95%LOA = 0.0001) (Fig 3). After excluding bone, the exclusion of muscle (mean error = -0.004, 95% LOA: 0.0001), and then blood (mean error = -0.006, 95% LOA: 0.0001) or adipose (mean error -0.004, 95% LOA: 0.0001) ROIs had a limited effect on the derived muscle density values. We completed the remainder of the analysis using two ROIs, adipose and air, which were easily identifiable and produced accurate muscle density values with the internal calibration method as described above.

We found that the muscle density values derived from the internal and reference sucrose water phantom calibration methods were highly correlated (R^2 > 0.99) (Fig 4). The internal muscle density calibration method slightly underestimated muscle density, but the error was low when compared to the reference sucrose water phantom method (< 0.006 g/cm^3) with only a 0.54% difference between the muscle density values derived from the two methods (Fig 3). We found that with increasing muscle density, the error associated with the internal calibration method diminished linearly (y-intercept = -0.01, slope = 0.006).

The mean CV for density of muscle samples across different scan protocols and positioning was significantly different across the internal calibration method, sucrose water phantom method, and native HU (p < 0.001) (Fig 5). The mean CV for density of the muscle samples was significantly greater the native HU (mean CV = 6.52%) when 1) compared to the internal muscle density calibration method (mean CV = 0.33%) (p < 0.001) and 2) compared to the
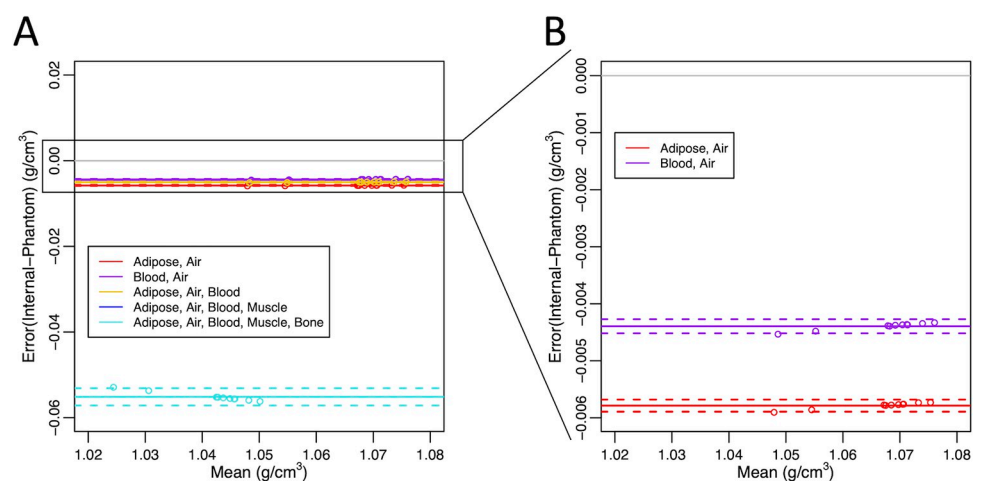
Fig 3. Bland-Altman plots comparing calibration methods. Bland-Altman plots comparing the differences between internal derived muscle density values and reference sucrose water phantom derived muscle density values (n = 10 muscle samples). Different combinations of regions of interest (ROIs) for the internal calibration method are represented in different colours. The mean differences are shown as solid lines and 95% limits of agreement are shown as dashed lines. A) Bland-Altman plot with all tested internal calibration ROI combinations. B) Bland-Altman plot with two internal calibration ROI combinations (air, adipose; air, blood).

https://doi.org/10.1371/journal.pone.0273203.g003

Fig 4. Regression plot comparing calibration methods. Regression plot comparing the muscle density values (n = 10 muscle sam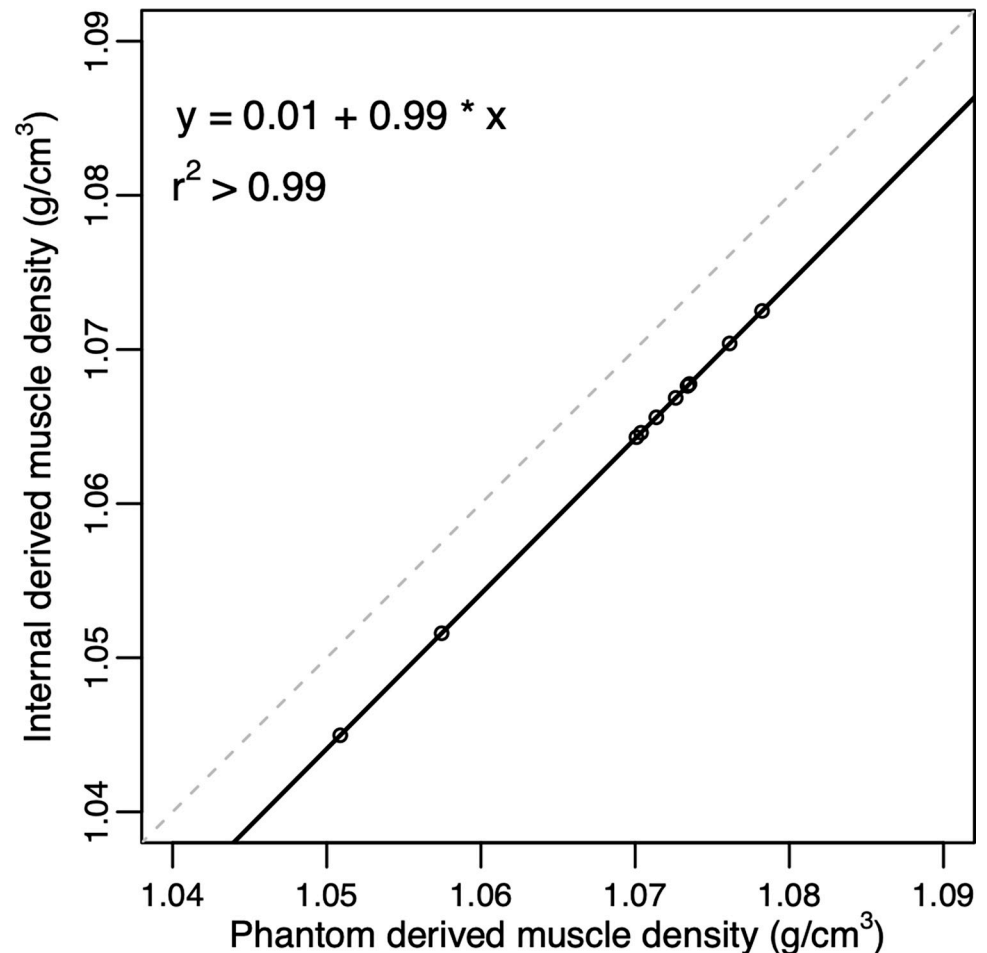ples) derived from the internal calibration method and the reference sucrose water phantom method. Solid line indicates regression line, dashed line indicates the line of unity.

reference sucrose water phantom calibration method (mean CV = 0.52%) (p < 0.001). There was no difference between the mean CV for density of the muscle samples derived from the internal calibration method and the reference sucrose water phantom calibration method (p = 1).

The HA bone phantom derived muscle density values were highly correlated with those derived from the reference sucrose water phantom calibration method (R^2 > 0.99) and the internal calibration method (R^2 > 0.99) (S1 Fig). However, the absolute values differed because the reference sucrose water phantom and internal calibration methods derive muscle density in g/cm^3, whereas the HA bone phantom derives muscle density values in mgHA/cm^3 (S2 Fig).

Discussion

We implemented and validated a previously established CT internal calibration method that estimates scan effective energy for muscle density analysis [32]. The results support our hypothesis that the internal muscle density calibration method is comparable to the reference sucrose water phantom calibration method. We also found that, as hypothesized, the internal
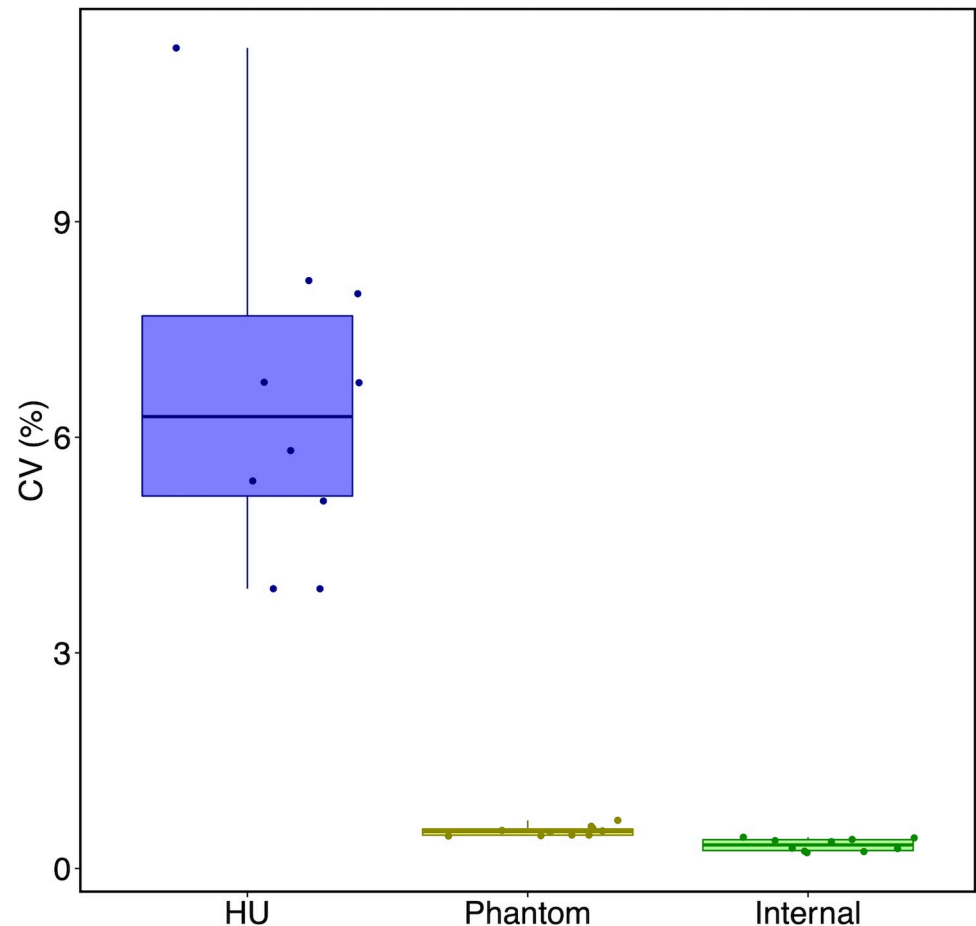
Fig 5. Boxplot comparing coefficient of variation (CV) values. Coefficient of variation (CV) for muscle density
(n = 10 muscle samples) values across different two scan protocols and five scan positions. The left boxplot represents
native Hounsfield units (HU). Muscle density values were derived from the reference sucrose water phantom
calibration method (middle boxplot) and the internal calibration method (right boxplot). Each box extends from the
25th percentile to the 75th percentile of the distribution of the respective values. The horizontal lines within each
box denote median values and the vertical lines outside the box denote the minimum and maximum values.

https://doi.org/10.1371/journal.pone.0273203.g005

calibration derived muscle density values were more robust than HU as demonstrated across 5
scan positions and 2 scan protocols.

We demonstrated that using air and adipose ROIs for the internal calibration method were
sufficient to yield accurate muscle density values when compared with the reference sucrose
water phantom calibration method. When bone was excluded as an ROI, there was a large
reduction in error associated with the internal calibration method. This error may have been
associated with tissue inhomogeneity within the bone ROI, paired with the high density of
bone relative to muscle. Inhomogeneity in cortical bone could affect the calculated slope of the
linear equation and result in drastic differences in perceived muscle values. Besides bone, we
excluded muscle as an internal calibration ROI to avoid bias in the output muscle density val-
ues. Blood was excluded as an ROI to simplify the methods and because the vessels are rela-
tively small, which makes it challenging to select regions composed only of blood. However,
blood could be used to substitute the adipose ROI if necessary. Our tests revealed that the
removal of muscle and blood ROIs did not greatly impact our measured muscle density values.
While optimal ROI selection may differ for BMD internal calibration, Lee et al. similarly

found that air and adipose (or blood) internal calibration ROIs produced precise BMD values [31]. This differs from other evaluations which used air, adipose, blood, skeletal muscle [39], and bone [32]. However, Bartenschlager et al. recently quantified accuracy error associated with different ROIs and ultimately suggested the use of air and subcutaneous adipose tissue or blood [40].

Consistent with BMD internal calibration studies, we found our internal muscle density calibration method resulted in muscle density values that were highly correlated with those produced by the phantom calibration method (in our study, the sucrose water phantom and the HA bone phantom) [31,32,41]. While our internal muscle density calibration method underestimated sucrose water phantom derived muscle density, the error was small ($< 1\%$) compared to clinical studies that have observed 10–40% differences in muscle attenuation between healthy controls and patients with hip osteoarthritis, fractures, or aortic disease [3,42,43]. We found that our internal calibration method was more accurate, when compared to the sucrose water phantom, with increasing density values. Hence, this method may be more accurate when applied to denser muscle. Nonetheless, our internal calibration method was significantly less sensitive to scan protocol and object positioning within the scanner bore when compared to native HU, which is how CT derived muscle density values are usually reported in the literature [7–9,14–17,44,45]. Similarly, other studies have noted inconsistencies in absolute HU values across scan protocols and positioning [11,18–23]. Therefore, rather than reporting native HU, we recommend an internal calibration procedure to convert to g/cm^3.

There are important limitations associated with our study. Notably, ex vivo bovine and swine tissue samples were scanned instead of human participants, which may have different tissue densities that influenced the internal calibration derived muscle density values. These samples do not account for differences in patient anatomy (i.e., patient size) which have been noted to impact resulting HU values [46–48]. However, the internal calibration approach utilized here should be less dependent on patient characteristics as reference values are taken from the patient themselves, which should account for patient-specific alterations in x-ray attenuation. Further, we utilized a sucrose water phantom due to the lack of standard phantoms for muscle density analysis. While we did not test stability of the phantom, the primary purpose of the phantom was for comparison with internal calibration rather than continued use of a phantom. For this study, we examined muscle density values for the same muscle sample across different scan positions and protocols. However, we did not examine derived muscle density values across different scanners or scan manufacturers, limiting the generalizability of our findings on internal calibration reliability.

Conclusions

We developed a new internal calibration method to measure muscle density from CT images that does not require calibration phantoms and is robust across scan protocols and positioning within the scanner bore. This internal calibration method will enable the secondary analysis of clinically acquired CT images to assess muscle density, a quantitative assessment of muscle quality, using an inexpensive method without exposure to additional ionizing radiation.

Supporting information

S1 Fig. Regression plot comparing calibration methods. Regression plots comparing the muscle density values derived from the hydroxyapatite (HA) bone phantom method with A) the reference sucrose water phantom method and B) the internal calibration method (n = 10

muscle samples). Solid line indicates regression line, dashed line indicates the line of unity.
(TIFF)

S2 Fig. Bland-Altman plots comparing calibration methods. Bland-Altman plots comparing
calibration methods. The mean differences are shown as solid lines and 95% limits of agree-
ment are shown as dashed lines. A) Bland-Altman plot comparing differences between internal
derived muscle density values and hydroxyapatite (HA) bone phantom derived muscle density
values (n = 10 muscle samples). B) Bland-Altman plot comparing differences between the
sucrose water phantom derived muscle density values and hydroxyapatite (HA) bone phantom
derived muscle density values (n = 10 muscle samples). Internal and sucrose water phantom
derived muscle density values are represented in g/cm^3. HA phantom derived muscle density
values are represented in $mgHA/cm^3$.
(TIFF)

**S1 File. Data used to generate Figs 3–5, S1 and S2, and mean and standard deviation values
reported.**
(XLSX)

S2 File. R markdown document with statistical analysis code and outputs.
(DOCX)

S3 File. R script files with statistical analysis code.
(ZIP)

S4 File. Internal calibration muscle density analysis code.
(ZIP)

S5 File. Image registration code.
(TXT)

Author Contributions

Conceptualization: Ainsley C. J. Smith, Justin J. Tse, Steven K. Boyd, Sarah L. Manske.

Data curation: Ainsley C. J. Smith, Sarah L. Manske.

Formal analysis: Ainsley C. J. Smith, Justin J. Tse, Tadiwa H. Waungana, Kirsten N. Bott,
 Michael T. Kuczynski, Sarah L. Manske.

Funding acquisition: Ainsley C. J. Smith, Justin J. Tse, Michael T. Kuczynski, Sarah L.
 Manske.

Investigation: Ainsley C. J. Smith, Justin J. Tse, Sarah L. Manske.

Methodology: Ainsley C. J. Smith, Justin J. Tse, Sarah L. Manske.

Project administration: Ainsley C. J. Smith, Justin J. Tse, Sarah L. Manske.

Resources: Ainsley C. J. Smith, Justin J. Tse, Michael T. Kuczynski, Andrew S. Michalski,
 Sarah L. Manske.

Software: Ainsley C. J. Smith, Tadiwa H. Waungana, Kirsten N. Bott, Michael T. Kuczynski,
 Andrew S. Michalski, Sarah L. Manske.

Supervision: Steven K. Boyd, Sarah L. Manske.

Validation: Ainsley C. J. Smith, Justin J. Tse, Sarah L. Manske.

Visualization: Ainsley C. J. Smith, Sarah L. Manske.

Writing – original draft: Ainsley C. J. Smith, Sarah L. Manske.

Writing – review & editing: Ainsley C. J. Smith, Justin J. Tse, Tadiwa H. Waungana, Kirsten N. Bott, Michael T. Kuczynski, Andrew S. Michalski, Steven K. Boyd, Sarah L. Manske.

References

1. Vanhorebeek I, Latronico N, Van den Berghe G. ICU-acquired weakness. Intensive Care Med. 2020; 46(4):637–53. https://doi.org/10.1007/s00134-020-05944-4 PMID: 32076765

2. Santilli V, Bernetti A, Mangone M, Paoloni M. Clinical definition of sarcopenia. Clin Cases Miner Bone Metab. 2014; 11(3):177–180. https://doi.org/10.11138/ccmbm/2014.11.3.177 PMID: 25568649

3. Rasch A, Byström AH, Dalen N, Berg HE. Reduced muscle radiological density, cross-sectional area, and strength of major hip and knee muscles in 22 patients with hip osteoarthritis. Acta Orthop. 2009; 78 (4):505–10. https://doi.org/10.1080/17453670710014158 PMID: 17966005

4. Tsukasaki K, Matsui Y, Arai H, Harada A, Tomida M, Takemura M, et al. Association of Muscle Strength and Gait Speed with Cross-Sectional Muscle Area Determined by Mid-Thigh Computed Tomography— A Comparison with Skeletal Muscle Mass Measured by Dual-Energy X-Ray Absorptiometry. J frailty aging. 2020; 9(2):82–9. https://doi.org/10.14283/jfa.2020.16 PMID: 32259181

5. Zuckerman J, Ades M, Mullie L, Trnkus A, Morin JF, Langlois Y, et al. Psoas Muscle Area and Length of Stay in Older Adults Undergoing Cardiac Operations. Ann Thorac Surg. 2017; 103(5):1498–504. https://doi.org/10.1016/j.athoracsur.2016.09.005 PMID: 27863730

6. Gomindes AR, Appleton JP, Chugh R, Welch C. Muscle Quantity at C3 and/or L3 on Routine Trauma Series Computed Tomography Correlate With Brain Frailty and Clinical Frailty Scale: A Cross-Sectional Study. Cureus. 2021; 13(6). https://doi.org/10.7759/cureus.15912 PMID: 34336420

7. Chu MP, Lieffers J, Ghosh S, Belch AR, Chua NS, Fontaine A, et al. Skeletal Muscle Radio-Density Is an Independent Predictor of Response and Outcomes in Follicular Lymphoma Treated with Chemoim-munotherapy. PLoS One. 2015; 10(6):e0127589. https://doi.org/10.1371/journal.pone.0127589 PMID: 26030144

8. Besutti G, Id MP, Ottone M, Id MC, Milic J, Bonelli E, et al. The impact of chest CT body composition parameters on clinical outcomes in COVID-19 patients. PLoS One. 2021; 16(5):e0251768. https://doi.org/10.1371/journal.pone.0251768 PMID: 33989341

9. Lú A, De Carvalho M, Cristina Gonzalez M, Matias De Sousa I, Amorim Das Virgens IP, Otavio G, et al. Low skeletal muscle radiodensity is the best predictor for short-term major surgical complications in gas-trointestinal surgical cancer: A cohort study. PLoS One. 2021; 16(2):e0247322. https://doi.org/10.1371/journal.pone.0247322 PMID: 33606786

10. Aubrey J, Esfandiari N, Baracos VE, Buteau FA, Frenette J, Putman CT, et al. Measurement of skeletal muscle radiation attenuation and basis of its biological variation. Acta Physiol (Oxf). 2014; 210(3):489. https://doi.org/10.1111/apha.12224 PMID: 24393306

11. Engelke K, Museyko O, Wang L, Laredo JD. Quantitative analysis of skeletal muscle by computed tomography imaging—State of the art. J Orthop Transl. 2018; 15:91–103. https://doi.org/10.1016/j.jot.2018.10.004 PMID: 30533385

12. Yamashita M, Kamiya K, Matsunaga A, Kitamura T, Hamazaki N, Matsuzawa R, et al. Prognostic Value of Psoas Muscle Area and Density in Patients Who Undergo Cardiovascular Surgery. Can J Cardiol. 2017; 33(12):1652–9. https://doi.org/10.1016/j.cjca.2017.10.009 PMID: 29173605

13. Wang L, Yin L, Zhao Y, Su Y, Sun W, Chen S, et al. Muscle Density, but Not Size, Correlates Well With Muscle Strength and Physical Performance. J Am Med Dir Assoc. 2021; 22(4):751–759.e2. https://doi.org/10.1016/j.jamda.2020.06.052 PMID: 32768372

14. Kim IH, Choi MH, Lee IS, Hong TH, Lee MA. Clinical significance of skeletal muscle density and sarco-penia in patients with pancreatic cancer undergoing first-line chemotherapy: a retrospective observa-tional study. BMC Cancer. 2021; 21(1). https://doi.org/10.1186/s12885-020-07753-w PMID: 33461517

15. Cortellini A, Bozzetti F, Palumbo P, Brocco D, Di Marino P, Tinari N, et al. Weighing the role of skeletal muscle mass and muscle density in cancer patients receiving PD-1/PD-L1 checkpoint inhibitors: a multi-center real-life study. Sci Rep. 2020; 10(1). https://doi.org/10.1038/s41598-020-58498-2 PMID: 31996766

16. Tokuda T, Yamamoto M, Kagase A, Koyama Y, Otsuka T, Tada N, et al. Importance of combined assessment of skeletal muscle mass and density by computed tomography in predicting clinical out-comes after transcatheter aortic valve replacement. Int J Cardiovasc Imaging. 2020; 36(5):929–38. https://doi.org/10.1007/s10554-020-01776-x PMID: 32040683

17. Yamashita M, Kamiya K, Matsunaga A, Kitamura T, Hamazaki N, Matsuzawa R, et al. Preoperative skeletal muscle density is associated with postoperative mortality in patients with cardiovascular disease. Interact Cardiovasc Thorac Surg. 2020; 30(4):515–22. https://doi.org/10.1093/icvts/ivz307 PMID: 31886866

18. Groell R, Rienmueller R, Schaffler GJ, Portugaller HR, Graif E, Willfurth P. CT number variations due to different image acquisition and reconstruction parameters: A thorax phantom study. Comput Med Imaging Graph. 2000; 24(2):53–8. https://doi.org/10.1016/s0895-6111(99)00043-9 PMID: 10767584

19. Levi C, Gray JE, McCullough EC, Hattery RR. The unreliability of CT numbers as absolute values. AJR Am J Roentgenol. 1982; 139(3):443–447. https://doi.org/10.2214/ajr.139.3.443 PMID: 6981306

20. Zerhouni EA, Spivey JF, Morgan RH, Leo FP, Stitik FP, Siegelman SS. Factors influencing quantitative CT measurements of solitary pulmonary nodules. J Comput Assist Tomogr. 1982; 6(6):1075–87. https://doi.org/10.1097/00004728-198212000-00005 PMID: 7174924

21. Maki DD, Birnbaum BA, Chakraborty DP, Jacobs JE, Carvalho BM, Herman GT. Renal Cyst Pseudoenhancement: Beam-hardening Effects on CT Numbers. Radiology. 1999; 213(2):468–472. https://doi.org/10.1148/radiology.213.2.r99nv33468 PMID: 10551228

22. Yushkevich PA, Piven J, Hazlett HC, Smith RG, Ho S, Gee JC, et al. User-guided 3D active contour segmentation of anatomical structures: Significantly improved efficiency and reliability. Neuroimage. 2006; 31(3):1116–28. https://doi.org/10.1016/j.neuroimage.2006.01.015 PMID: 16545965

23. Mühlberg A, Museyko O, Laredo JD, Engelke K. A reproducible semi-automatic method to quantify the muscle-lipid distribution in clinical 3D CT images of the thigh. PLoS One. 2017; 12(4):e0175174. https://doi.org/10.1371/journal.pone.0175174 PMID: 28453512

24. Faulkner KG, Glüer CC, Grampp S, Genant HK. Cross-calibration of liquid and solid QCT calibration standards: corrections to the UCSF normative data. Osteoporos Int. 1993; 3(1):36–42. https://doi.org/10.1007/BF01623175 PMID: 8422515

25. Engelke K, Lang T, Khosla S, Qin L, Zysset P, Leslie WD, et al. Clinical Use of Quantitative Computed Tomography–Based Advanced Techniques in the Management of Osteoporosis in Adults: the 2015 ISCD Official Positions—Part III. J Clin Densitom. 2015; 18(3):393–407. https://doi.org/10.1016/j.jocd.2015.06.010 PMID: 26277853

26. Mühlberg A, Museyko O, Bousson V, Pottecher P, Laredo JD, Engelke K. Three-dimensional Distribution of Muscle and Adipose Tissue of the Thigh at CT: Association with Acute Hip Fracture. Radiology. 2019; 290(2):426–434. https://doi.org/10.1148/radiol.2018181112 PMID: 30457478

27. Cann CE, Genant HK. Precise measurement of vertebral mineral content using computed tomography. J Comput Assist Tomogr. 1980; 4(4):493–500. https://doi.org/10.1097/00004728-198008000-00018 PMID: 7391292

28. Wong AKO, Merali Z, Adachi JD. Development of a Skeletal Muscle Mimic Phantom Compatible with QCT and MR Imaging. J Med Imaging Radiat Sci. 2015; 46(2):174–81. https://doi.org/10.1016/j.jmir.2014.10.002 PMID: 31052091

29. Adams AL, Fischer H, Kopperdahl DL, Lee DC, Black DM, Bouxsein ML, et al. Osteoporosis and Hip Fracture Risk From Routine Computed Tomography Scans: The Fracture, Osteoporosis, and CT Utilization Study (FOCUS). J Bone Miner Res. 2018; 33(7):1291–301. https://doi.org/10.1002/jbmr.3423 PMID: 29665068

30. Fidler JL, Murthy NS, Khosla S, Clarke BL, Bruining DH, Kopperdahl DL, et al. Comprehensive assessment of osteoporosis and bone fragility with ct colonography. Radiology. 2016; 278(1):172–80. https://doi.org/10.1148/radiol.2015141984 PMID: 26200602

31. Lee DC, Hoffmann PF, Kopperdahl DL, Keaveny TM. Phantomless calibration of CT scans for measurement of BMD and bone strength—Inter-operator reanalysis precision. Bone. 2017; 103:325–33. https://doi.org/10.1016/j.bone.2017.07.029 PMID: 28778598

32. Michalski AS, Besler BA, Michalak GJ, Boyd SK. CT-based internal density calibration for opportunistic skeletal assessment using abdominal CT scans. Med Eng Phys. 2020; 78:55–63. https://doi.org/10.1016/j.medengphy.2020.01.009 PMID: 32059948

33. Chen J, Moir D. An estimation of the annual effective dose to the Canadian population from medical CT examinations. J Radiol Prot. 2010; 30(2):131–7. https://doi.org/10.1088/0952-4746/30/2/002 PMID: 20530855

34. Berdahl CT, Vermeulen MJ, Larson DB, Schull MJ. Emergency department computed tomography utilization in the United States and Canada. Ann Emerg Med. 2013; 62(5). https://doi.org/10.1016/j.annemergmed.2013.02.018 PMID: 23683773

35. Mattes D, Haynor DR, Vesselle H, Lewellyn TK, Eubank W. Nonrigid multimodality image registration. Med Imaging 2001 Image Process. 2001; 4322:1609–20. https://doi.org/10.1117/12.431046

36. Schroeder W, Martin K, Lorensen B. The visualization toolkit: an object-oriented approach to 3D graphics. 4th ed. 2006.

37. Lowekamp BC, Chen DT, Ibáñez L, Blezek D. The Design of SimpleITK. Front Neuroinform. 2013; 7:45. https://doi.org/10.3389/fninf.2013.00045 PMID: 24416015

38. Harris CR, Millman KJ, van der Walt SJ, Gommers R, Virtanen P, Cournapeau D, et al. Array programming with NumPy. Nat. 2020; 585(7825):357–62. https://doi.org/10.1038/s41586-020-2649-2 PMID: 32939066

39. Winsor C, Li X, Qasim M, Henak CR, Pickhardt PJ, Ploeg H, et al. Evaluation of patient tissue selection methods for deriving equivalent density calibration for femoral bone quantitative CT analyses. Bone. 2021;143. https://doi.org/10.1016/j.bone.2020.115759 PMID: 33212317

40. Bartenschlager S, Dankerl P, Chaudry O, Uder M, Engelke K. BMD accuracy errors specific to phantomless calibration of CT scans of the lumbar spine. Bone. 2022; 157:116304. https://doi.org/10.1016/j.bone.2021.116304 PMID: 34973497

41. Boomsma MF, Slouwerhof I, Van Dalen JA, Edens MA, Mueller D, Milles J, et al. Use of internal references for assessing CT density measurements of the pelvis as replacement for use of an external phantom. Skeletal Radiol. 2015; 44(11):1597–1602. https://doi.org/10.1007/s00256-015-2206-5 PMID: 26173417

42. Wang L, Yin L, Zhao Y, Su Y, Sun W, Liu Y, et al. Muscle density discriminates hip fracture better than computed tomography X-ray absorptiometry hip areal bone mineral density. J Cachexia Sarcopenia Muscle. 2020; 11(6):1799–812. https://doi.org/10.1002/jcsm.12616 PMID: 32894000

43. Yamashita M, Kamiya K, Matsunaga A, Kitamura T, Hamazaki N, Ichikawa T, et al. Features of trunk muscle wasting during acute care and physical function recovery with aortic disease. J Cachexia Sarcopenia Muscle. 2022; 13(2):1054–1063. https://doi.org/10.1002/jcsm.12935 PMID: 35178890

44. Looijaard WGPM Dekker IM, Beishuizen A Girbes ARJ, Oudemans-van Straaten HM Weijs PJM. Early high protein intake and mortality in critically ill ICU patients with low skeletal muscle area and -density. Clin Nutr. 2020; 39(7):2192–201. https://doi.org/10.1016/j.clnu.2019.09.007 PMID: 31669003

45. Vella CA, Nelson MC, Unkart JT, Miljkovic I, Allison MA. Skeletal muscle area and density are associated with lipid and lipoprotein cholesterol levels: The Multi-Ethnic Study of Atherosclerosis. J Clin Lipidol. 2020; 14(1):143. https://doi.org/10.1016/j.jacl.2020.01.002 PMID: 32061531

46. Sodickson A, Weiss M. Effects of patient size on radiation dose reduction and image quality in low-kVp CT pulmonary angiography performed with reduced IV contrast dose. Emerg Radiol. 2012; 19(5):437–445. https://doi.org/10.1007/s10140-012-1046-z PMID: 22527361

47. Ogden K, Huda W, Scalzetti EM, Roskopf ML. Patient size and x-ray transmission in body CT. Health Phys. 2004; 86(4):397–405. https://doi.org/10.1097/00004032-200404000-00009 PMID: 15057061

48. Zheng X, Al-Hayek Y, Cummins C, Li X, Nardi L, Albari K, et al. Body size and tube voltage dependent corrections for Hounsfield Unit in medical X-ray computed tomography: theory and experiments. Sci Reports. 2020; 10(1):1–10. https://doi.org/10.1038/s41598-020-72707-y PMID: 32973237